Extended Methods of Emission Spectroscopy for the Analysis of Arc Dynamics and Arc Interaction with Walls

Uhrlandt D., Methling R., Franke St., Gorchakov S., Baeva M., Khakpour A., Brüser V.

Leibniz Institute for Plasma Science and Technology (INP Greifswald), Felix-Hausdorff-Str. 2, 17489 Greifswald, Germany, uhrlandt@inp-greifswald.de

Recently, a number of improved methods of optical emission spectroscopy have been proposed for the study of high-current arcs with special emphasis on the treatment of optical thick arc radiation and analysis of the arc dynamics. The paper gives a short review on these methods focusing on the determination of plasma properties by means of comparison of measured and simulated emission spectra and the use of high-speed video spectroscopy. The application of these methods is demonstrated for a specific example; the study of the interaction of arcs with side walls and the impact of ceramic coatings on the wall's protection. For that purpose, a free burning arc experiment with CuW electrodes is used. The strong electrode erosion causes the arc operation in copper vapour with high stability and reproducibility. The arc temperature profile is obtained from measurements of copper line radiation complemented with radiation transport simulations. The impact of the arc radiation on the evaporation of different ceramic coatings of side walls is studied by video spectroscopy. The resulting impact on the heat load of the walls is derived from thermographic measurements.

Keywords: optical emission spectroscopy, plasma temperature, arc wall interaction

1 INTRODUCTION

Optical emission spectroscopy (OES) has been established as a main diagnostic method for the study of thermal plasmas and the determination of plasma properties like plasma temperature and densities of emitting species as long as the plasma is optically accessible. These measurements are preferentially used for the validation of plasma models. The intense radiation of arcs in the visible range allows measurements with low acquisition time and in small spectral ranges. This would make possible, in general, the study of arcs with high temporal dynamics and high accuracy. However, most of the established methods are limited by a number of required assumptions and other boundary conditions for the radiation analysis.

On the one hand, recording techniques with high temporal resolution (use of photomultiplier or fibre spectrometer) have typically no or low spatial resolution (see e.g. [1]) whereas spatial imaging spectroscopy with intensified charge coupled device (ICCD) cameras are very limited in the repetition time (see e.g. [2]. Imaging spectroscopy coupled with a high speed camera (HSC) (here and later called video spectroscopy) offers an answer to this problem but is not well proven up to now.

One the other hand, most of the established methods are based on the analysis of line radiation and require an adequate knowledge of specific properties of the radiating species and their atomic transitions in the considered plasma. Methods like single-line or multiple-line analysis and analysis of the line profile width (see e.g. [3]) are limited to line radiation of low optical thickness and plasma temperatures below the normal maximum of the lines. The latter describes the point of maximum intensity before the intensity decreases with increasing temperature due to a significant decrease of the radiator density according to the change of the plasma composition.

The most methods are based on the assumption of local thermodynamic equilibrium (LTE) of the plasma. Furthermore, rotational symmetry of the arc is assumed for the required spatial reconstruction of the local emission coefficient from side-on measurements from only one viewing angle. An exception is the Bartel's method for the evaluation of line radiation showing self-reversal [4]. Here, the plasma temperature can be obtained from the intensity of the side-on measured radiance in the maximum of the line profile with self-reversal. However, the method can fail in the temperature range above the normal maximum.

An alternative to the methods mentioned

above is to start with an assumption of spatial profiles of plasma temperature and radiator densities and applying simulations of side-on spectra by radiation transport calculations (see e.g. [5]). The comparison with calibrated measurements allows the successive improvement of the initial assumptions. This method will be discussed in more detail in section 2.

In view of the recently increased interest on studies of arc interaction with surfaces (electrodes and side walls), in sections 3 to 5 both methods, the temperature determination by radiation transport calculations and side-on measured spectra and the video spectroscopy, will be demonstrated on the example of a free burning arc experiment considering the evaporation of protective layers of side walls. A specific setup with WCu and W electrodes, as described in section 3, provides arcs dominated by the copper evaporation at the cathode which show high stability and reproducibility.

Studies of the electrode erosion in arc applications have a long history because this process is a key issue for lifetime and reliability. The same holds for the study of nozzle ablation in high-voltage circuit-breakers focussing mainly on polytetrafluoroethylene (PTFE) [6]. More recently, the replacement of PTFE by other gas-producing polymeric materials has been studied [7-11]. Some of these studies concern also the unintentional and often crucial evaporation of side walls, e.g. in low-voltage circuit-breakers. The possible protection of side walls against heat load and erosion by means of appropriate coatings represents an additional aspect. For example, ceramic coatings offer additional advantages because there are cheap, easy coating techniques are available, and the coating can be partially regenerated from the evaporation products. First studies of the arc interaction with ceramic coatings have been presented in a preceding paper [12]. In this paper, more robust coatings as well as improved diagnostic methods for the analysis of the arc and the evaporation of the coatings are considered.

2 OES AND RADIATION TRANSPORT

OES of line radiation from metal vapours (Fe, Cu, Mg) can be well used for temperature determination in arcs in different gases. The large variety of metal lines in the visible spectrum makes it easy to find lines of atoms and ions or lines corresponding to optical transitions from quite different energy levels in small wavelength ranges which can be recorded simultaneously with high resolution. Boltzmann-plot of line intensities or the ratio of atomic and ionic lines is well applicable as long as the vapour concentration and consequently the optical thickness of the lines are sufficiently low. In contrast to that, lines of broad profiles with large overlapping and often self-reversal can be found in arcs which are dominated by metal vapour [13]. The line emission is accompanied by a significant absorption of the emitted radiation in the near and far surrounding of every emission point. The radiation transport affects the radiation intensity observed from outside as well as the power balance of the arc considerably.

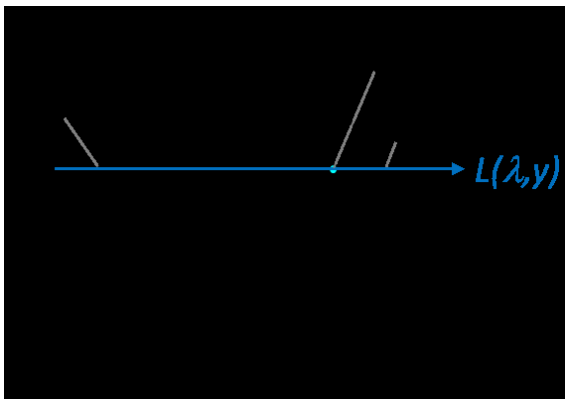

Fig. 1: Scheme of the line of sight (blue) through a plasma cross section (black circle) at the side-on position y

The solution of the radiation transport equation along a line of sight through the arc plasma enables a strict treatment of emission and absorption (see e.g. [5,14]). Let us consider a line of sight along direction x through the plasma at a side-on position y. This situation is illustrated in Fig. 1 for the case of cylindrical plasma which is observed from the side perpendicular to the cylinder axis. The position x varies between $-x_0$ and x_0 at the borders of the plasma. The spectral radiance L resulting from this line at the wavelength λ is determined by

$$L(\lambda, y) = \int_{-x_0}^{x_0} \varepsilon(\lambda, x, y) \exp\left[-\int_{x'}^{x_0} \kappa(\lambda, x', y) \mathrm{d}x'\right] \mathrm{d}x \quad (1).$$

$\varepsilon(\lambda, x, y)$ and $\kappa(\lambda, x, y)$ are the local spectral emission and absorption coefficients, respectively. In what follows the x- and y-dependence in ε- and κ-notations is dropped for the sake of simplicity. In both coefficients contributions from spectral lines (bound-bound transitions) and from continuum radiation have to be included. The emission coefficient of a line corresponding to the transition between atomic (ionic) levels k and i reads

$$\varepsilon_{ki}^{0}(T) = \frac{hc}{4\pi\lambda_{ki}} A_{ki} n_k(T) \quad (2)$$

with the central wavelength λ_{ki}, the transition probability A_{ki} , the speed of light c, the Planck constant h, and the density n_k of the upper excited level. Assuming LTE this density can be expressed by the Boltzmann distribution

$$n_k(T) = n_0(T) \frac{g_k}{Z(T)} \exp\left(-\frac{E_k}{kT}\right) \quad (3)$$

where n_0 is the total species density (atom or ion density for example), g_k is the statistical weight and E_k the excitation energy of the level, k - the Boltzmann constant, T - the temperature and $Z(T)$ - the partition function. The corresponding contribution to the spectral emission coefficient is calculated assuming, e.g., a Lorentz line profile with a half half-width λ_w^{ki} and line shift $\Delta\lambda_{ki}$ according to

$$\varepsilon_{ki}(\lambda, x) = \varepsilon_{ki}^{0} \frac{\lambda_w^{ki}}{\pi} \frac{1}{(\lambda - \lambda_{ki} - \Delta\lambda_{ki})^2 + (\lambda_w^{ki})^2} \quad (4)$$

where the values of T, $Z(T)$ and $n_0(T)$ are taken at the position x. The species densities result from plasma composition calculations for the respective local temperature and gas pressure applying the Gibbs-free energy minimization method. The corresponding absorption coefficient is calculated applying the Kirchhoff's law

$$\kappa_{ki}(\lambda, x) = \varepsilon_{ki}(\lambda, x) B_{\lambda_{ki}} \quad (5)$$

with the Planck function $B_{\lambda_{ki}}$.

In the example which will be presented in section 4, the radiation of the arc plasma in a copper-air mixture is considered in a spectral range from 490 to 530 nm for temperatures from 1 up to 20 kK. Here, 13 lines of Cu I (copper atoms), 108 lines of Cu II (singly ionized copper) and in addition a number of lines of oxygen and nitrogen (atoms and ions) are included with atomic data from the Kurucz and NIST Atomic Spectra Database each characterized with a Lorentz line profile. Each line width comprises a base part λ_w^{min} and a part from Stark broadening λ_w^{S} estimated according to [14-16]. The bremsstrahlung continuum (free-free transitions) and the recombination continuum (free-bound transitions) have been calculated as given in [14] using photoionization cross sections from [17, 18] and momentum transfer cross sections from [19].

As a first assumption for the considered example, a rotational symmetric temperature profile is constructed on the base of radial profiles of measured line intensities. Because the line intensities show mainly a box like profile with a quite flat central region, a temperature profile with a flat centre and a larger slope at outer positions is assumed. Then, the maximum temperature is adjusted by comparing with the measured intensities of Cu I lines at the central side-on position.

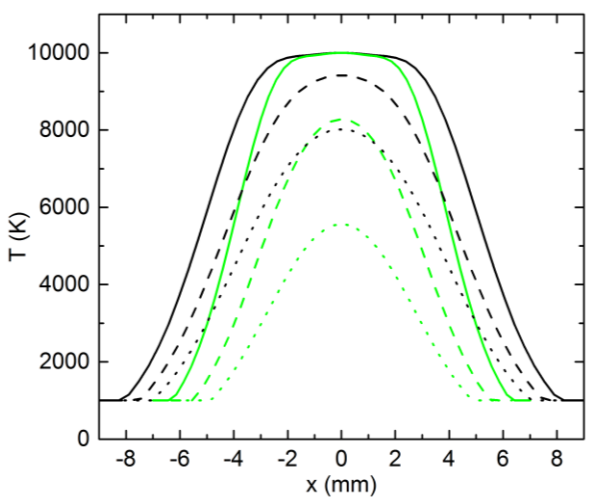

Fig. 2: Examples of considered radial arc temperature profiles (in green and black): temperature along the line of sight for the central side-on position (solid lines) and for side-on positions y=3 mm (dashed lines) and y=4 mm (dotted lines) from the arc axis

Examples of considered temperature profiles are shown in Fig. 1 considering a maximum temperature of 10 kK. Results of simulations of the side-on radiance L at the central side-on

position (y=0) for different maximum temperatures (12 and 15 kK) considering a copper vapour pressure of 1 bar (without contributions of air) and a radial temperature profile corresponding to the black profile in Fig. 2 are shown in Fig. 3. The spectral radiance is dominated by Cu I lines at λ_0=507.6, 510.6 and 515.3 nm where the last two show strong self-reversal. Cu II lines at λ_0=506.5 and 508.8 nm become visible at 15 kK maximum temperature.

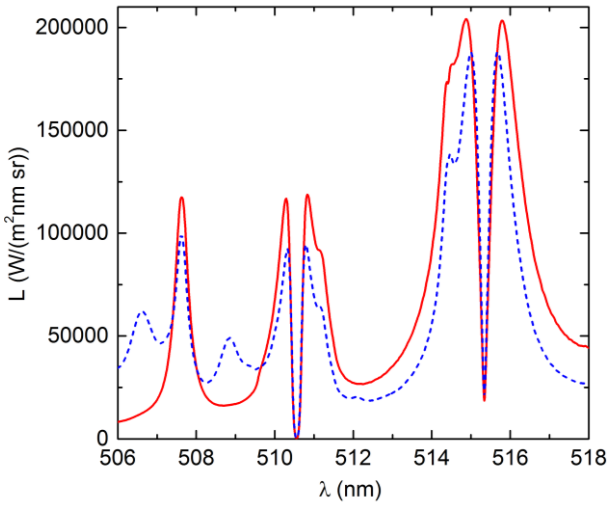

Fig. 3: Examples of radiance simulations for the radial temperature profile similar to the black curve in Fig. 1 but maximum temperatures 12 kK (red solid line) and 15 kK (blue dashed line) for the central side-on position

In the next step, the copper vapour pressure is adjusted mainly by comparing the line profile width of leading lines. Finally, the width of the temperature profile and in addition a radial profile of the copper vapour density is adjusted to find best agreement between simulation and measurements including several side-on positions. The results are presented in section 4.

3 EXPERIMENTAL STUDY OF ARC INTERACTION WITH PROTECTIVE COATINGS

An experimental setup in open air with road electrodes of 10 mm diameter, placed in a distance of 70 mm as shown in Fig. 4, is used for the operation of the arc. The lateral surface of the road electrodes is insulated by means of ceramic nozzles in order to fix the arc attachment area, and therefore, the current density at the electrode surfaces. A tungsten-copper electrode is used on the one side (the cathode in the first pulse), and a tungsten electrode on the other side (different from the setup in preceding studies [12]).

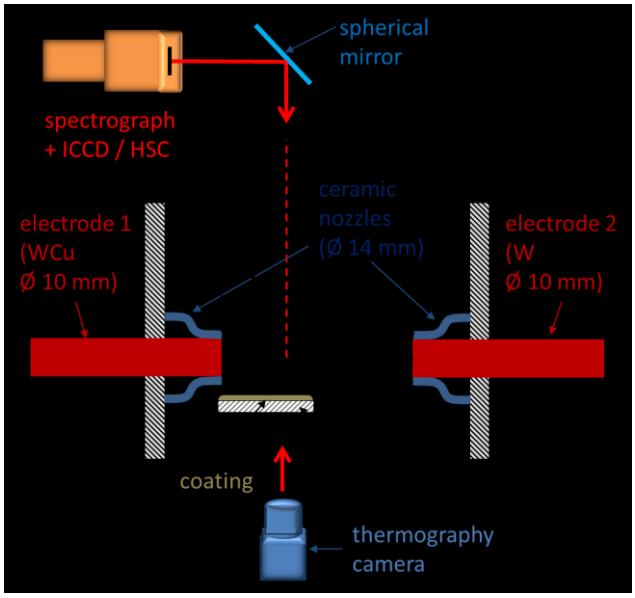

Fig. 4: Setup of the arc experiment

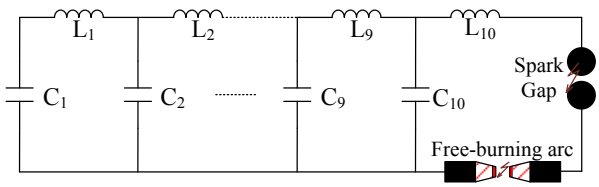

Fig. 5: Electrical circuit arrangement

Nearly rectangular current pulses are produced by means of a circuit shown in Fig. 5. LC elements with constant capacity of about 260 µF and stepwise decreasing inductances from L_1=610 µH to L_{10}=180 µH are coupled in series to produce pulses of about 5 ms duration and a peak current of 5.2 kA (first pulse). A spark gap is used for triggering. The arc in the setup shown in Fig. 3 is ignited using a thin copper wire between the electrodes.

Ceramic substrates of 1 mm thickness are arranged sideward to the arc in a distance of about 10 mm to the arc axis. The substrates are coated with ceramic materials $CaCO_3$ or $MgCO_3$ mixed either with plaster or with an organic binder. A sample of a coated plate is shown in Fig. 6. The arc causes typically a strong evaporation of the coating already during the first pulse.

Fig. 6: Example of a ceramic substrate coated with $CaCO_3$ and plaster

Examples of the measured courses of arc current, voltage and power are shown in Fig. 7. Only the first pulse with the maximum power is considered in the arc analysis. The impacts of the later pulses on the substrates are expected to be much lower. The voltage is a slightly higher in the case with $MgCO_3$ coating because of the vapour impact on the arc conductivity. However, the variation is comparable with the deviations between experiments with the same substrate and coating. Hence, a systematic change of the voltage could not be determined from the experiments.

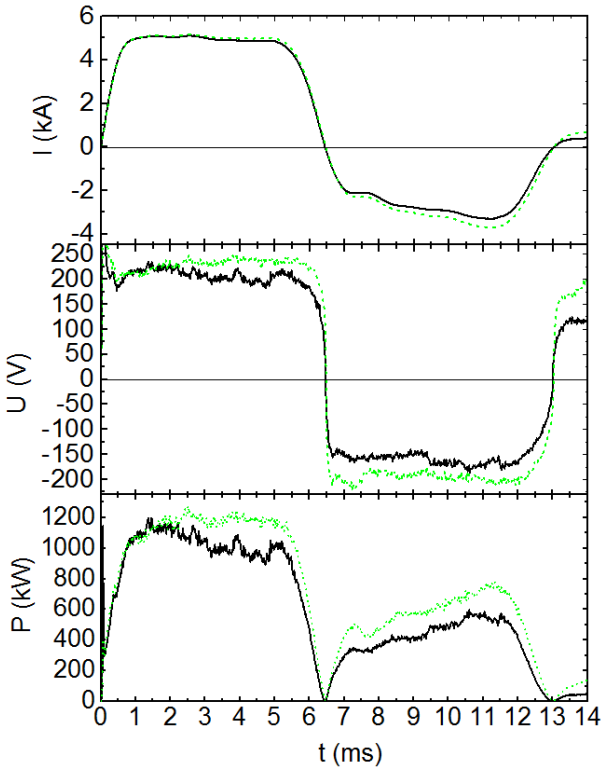

Fig. 7: Examples of arc current I, voltage U and power P for experiments with a ceramic substrate without coating (green dotted lines) and with $MgCO_3$ + plaster coating (black solid lines)

The arc radiation is recorded by a spectroscopic system consisting of a 0.5 m spectrograph either coupled with an ICCD (for one 2D image in one experiment) or a HSC (for video spectroscopy). A spherical mirror is used to image the cross section of the arc at a distance of 15 mm far from the electrode (cathode in the first pulse) on the slit of the spectrograph (see Fig. 3). A 1800 mm^{-1} grating is applied to record spectral ranges of 12 nm width around different wavelength positions (425, 512, 656 and 744 nm). The ICCD is typically triggered at 4 ms after arc ignition with exposure times between 1 and 5 µs. The HSC at the spectrograph is operated typically with a repetition rate of 4000 frames/s.

An additional colour HSC (not shown in Fig. 4) is used to observe the arc experiment with a repetition rate of 5000 frames/s. Example images recorded 4 ms after arc ignition during the first pulse are shown in Fig. 8. The electrodes are indicated by red lines. The cathode is on the left-hand side. The stable arc, at least near the cathode, caused by the cathode evaporation is illustrated in the case without coating (part (a) of Fig. 8). The impact of the coating evaporation becomes clearly visible in part (b) of Fig. 8.

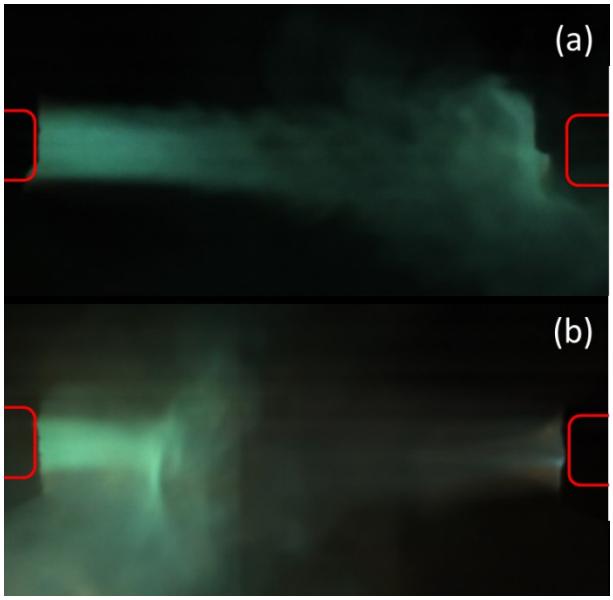

Fig. 8: Arc images at the instant 4 ms after ignition for the case without coating (a) and with $MgCO_3$ + plaster coating (b)

Fig. 9 shows an example of a 2D spectral radiance recorded by the ICCD in the wavelength range from 506 to 518 nm (abscissa) after intensity and wavelength calibration. The side-on position over the arc cross section is the ordinate.

The setup is completed by a thermography camera (see Fig. 4) with a spectral sensitivity

range from 7.5 to 12 µm. The camera is used to observe the backside of the coated substrates with a repetition rate of 50 frames/s. An image is shown in Fig. 10. Again, the electrodes (covert by other parts) are indicated by red lines. The yellow region shows the backside of the ceramic substrate, partly covert by the sample holder. The image range marked by the black frame is used to determine an averaged surface temperature of the substrate back side and its temporal evolution after the arc impact.

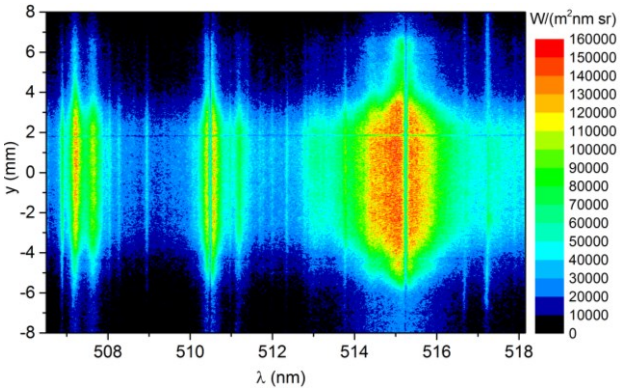

Fig. 9: 2D image of the arc spectral radiance for an axial position 15 mm away from the cathode recorded 4 ms after arc ignition in the case with $MgCO_3$ + plaster coating

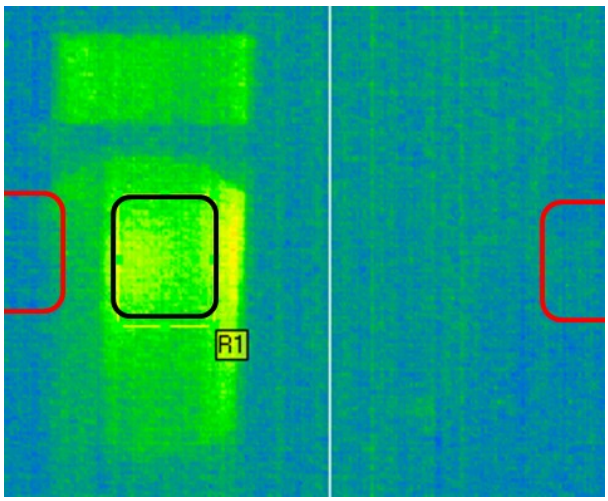

Fig. 10: Image of the thermography camera after arc impact in the case of a substrate with $MgCO_3$ + plaster coating

4 RESULTS FOR THE ARC PROPERTIES

The temperature profile of the copper vapour dominated arc is determined based on the spectral radiance measurements recorded at the instant 4 ms after arc ignition (see the example in Fig. 9). Results of the measurements for the central side-on position (y=0) are shown in Fig. 11 for three cases. In spite of the different substrate coatings, the spectral radiances are very similar in the considered spectral range. There are dominated by Cu I lines at 510.6 and 515.3 nm (central wavelength each) which show significant self-reversal as expected from the simulations shown in Fig. 3. In addition, a number of other lines without self-reversal in the range from 507 to 508 nm and at 511.3 nm are significant. Notice, that not all lines in the recorded spectrum could be successfully identified because of lack of data. Mg I lines become visible in case of the $MgCO_3$ + plaster coating in the range above 516 nm. This is an indication for the pronounced evaporation of the coating in this case.

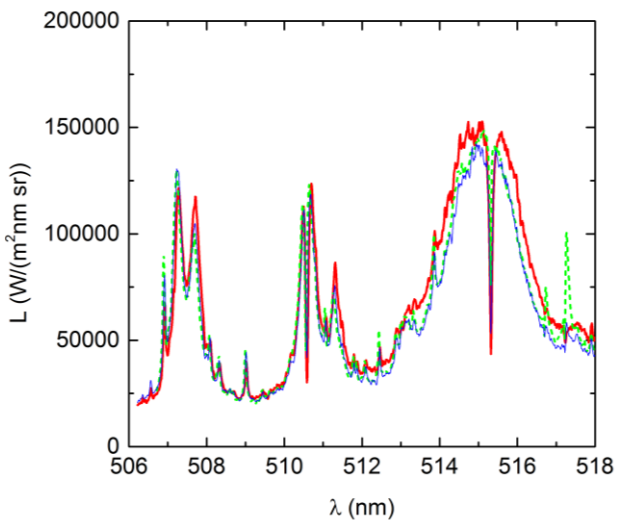

Fig. 11: Measured and calibrated spectral radiance L for y=0 for the cases of the substrate without coating (solid red line), with $MgCO_3$ + organic binder coating (thin solid blue line), and with $MgCO_3$ + plaster coating (dashed green line)

Only small deviations in the arc temperature profiles in the three cases are expected because of the similarities of the measured radiances. Therefore, radiation transport calculations as explained in section 2 are used to determine a typical arc temperature profile and a typical profile of the Cu density of the established arc during the first current pulse. Rotational symmetry is assumed. Fig. 12 shows simulation results for the spectral radiance based on the broader temperature profile in Fig. 2 but with peak temperatures of 9 and 10 kK in comparison with one of the measurements. A partial pressure of the copper vapour of 1 bar is assumed in the arc centre with a gradual radial decrease as explained below.

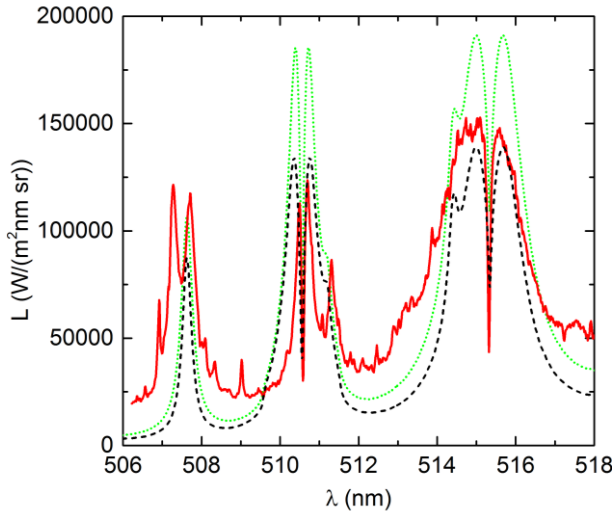

Fig. 12: Spectral radiance L for y=0 simulated for temperature profiles with the peak temperature 10 kK (dotted green line) and 9 kK (dashed black line) and measured in case of a substrate without coating (red solid line)

The absolute intensity of the Cu I lines can be well simulated when choosing a maximum temperature of 9 kK. The self-reversal and the width of the Cu I line at 515.3 nm is sufficiently reproduced by the choice of the broader radial profile. Remaining discrepancies result from additional lines which are not included in the simulation because of lack of data and from an insufficient description of the line broadening in case of the line at 510.6 nm.

Finally, the temperature profile and the profile of the partial pressure of copper given in Fig. 13 have been considered as the best choice after variation and comparison with measured radiances at different side-on positions. Fig. 14 gives an example for the comparison at the side-on position *y*=3 mm. Again, intensities and widths of the leading lines are reproduced sufficiently well by the simulation. The spectral radiance corresponding to the maximum of the left-hand wing of the dominant self-reversed Cu I line (around 515 nm) over the arc cross section is shown in Fig. 15 for the three cases considered above. Such values have been obtained from averaging the 2D images (see Fig. 9) over a small spectral range. The comparison with simulation results for few side-on positions shows a quite good agreement. Notice, that the relatively narrow pressure profile of copper have been chosen in order to simulate successfully the spatial profile (see Fig. 15 for example) as well as the inner shape of the self-reversed lines.

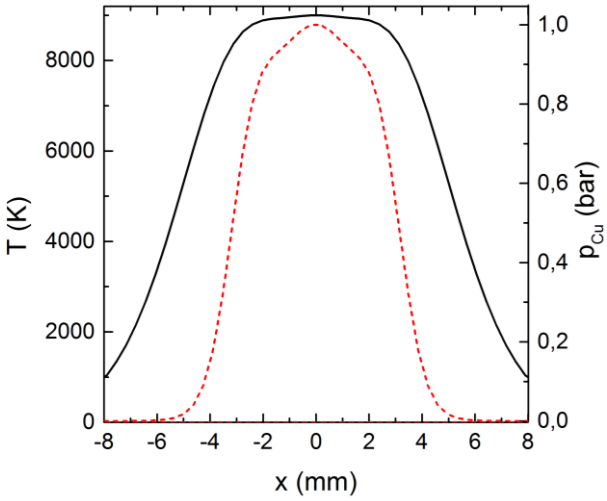

Fig. 13: Typical profiles of the plasma temperature (solid black line) and the copper partial pressure (dashed red line) of the considered arc

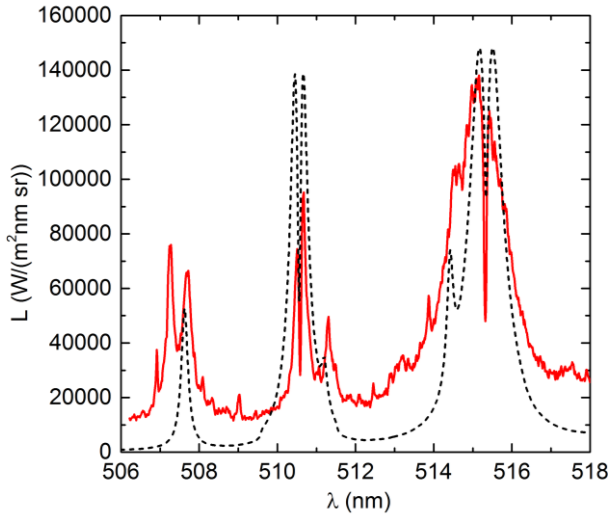

Fig. 14: Spectral radiance L for y=3 mm simulated for the temperature and pressure profiles in Fig. 13 (dashed black line) and measured in case of a substrate without coating (red solid line)

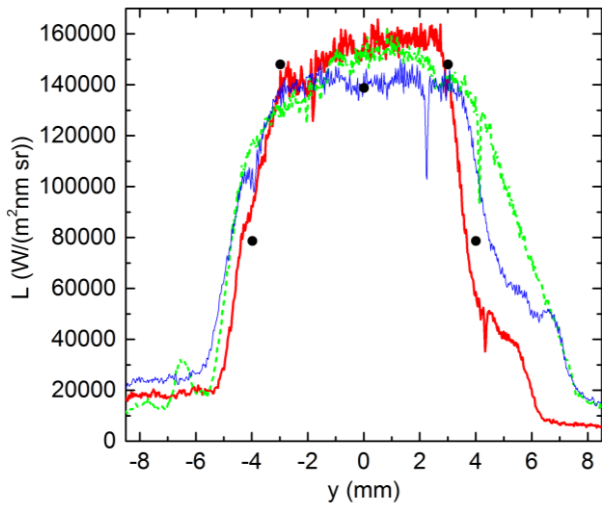

Fig. 15: Spectral radiance L for about 515 nm (maximum of the left-hand wing of the Cu I line at 515,3 nm) measured in the three cases given in Fig. 11 as a function of the side-on position y (lines) and from simulations for few side-on positions (solid circles)

Additional estimations become possible based on the rough determination of the arc temperature profile and the copper vapour pressure (see Fig. 13). For simplicity, a homogeneous cylindrical arc in poor copper with a radius of 5 mm and a temperature of 9 kK can be assumed. A net emission coefficient of $1{,}29\times10^{9}$ $Wm^{-3}sr^{-1}$ for such plasma has been calculated in [20]. A total emitted radiation of about 44 kW is obtained considering the arc length of 70 mm which is about 4 % of the typical power during the first pulse (see Fig. 7). Assuming homogeneous distribution of the emitted radiation in radial direction and full absorption at the substrates in a distance of 10 mm from the arc axis, an energy density of 10 MWm^{-2} is achieved characterizing the thermal load of the coatings during the first current pulse.

5 IMPACT OF PROTECTIVE COATINGS

The thermal load of the samples (substrates with coating) results in a more or less pronounced evaporation of the coating accompanied by a heating of the substrates. The evaporation can be qualitatively estimated by HSC images as shown for example in Fig. 8. A pronounced evaporation has been found in the case of both coatings $CaCO_3$ and $MgCO_3$ with plaster. The vapour flows into hot regions of the arc and causes quite visible emission of Ca and Mg, respectively.

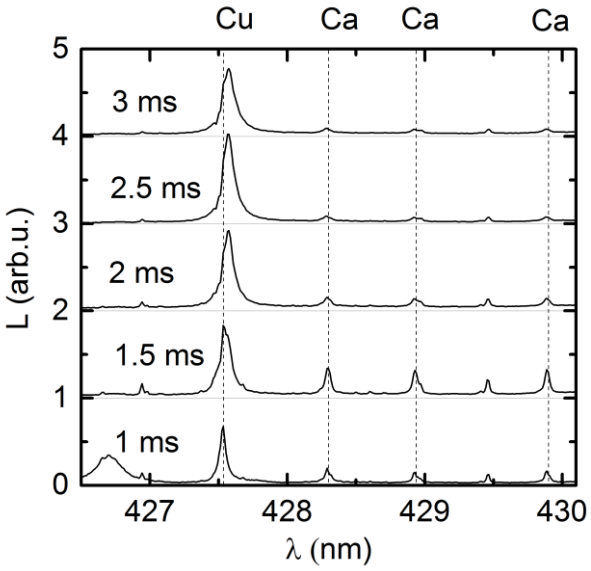

Fig. 16: Temporal evolution of the spectral radiance L for y=0 in the range of Ca I lines in case of the coating $CaCO_3$ + organic binder. The curves are presented with an offset increased by 1 with each time step of 0.5 ms

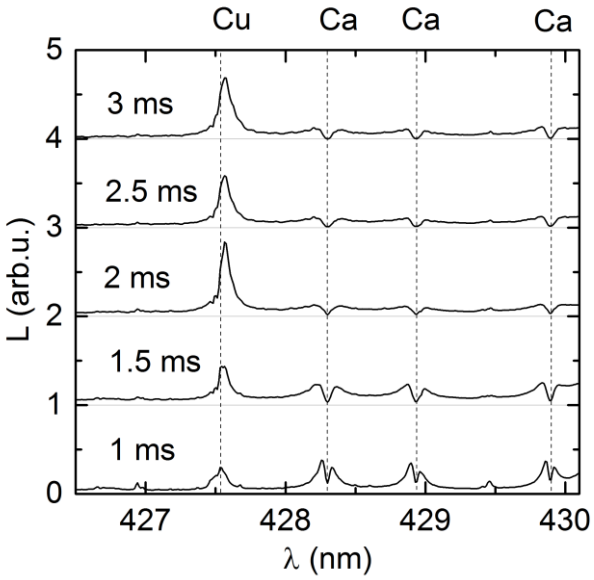

Fig. 17: Temporal evolution of the spectral radiance L for y=0 as in Fig. 16 but for a in the range of Ca I lines in case of the coating $CaCO_3$ + plaster

A quantitative analysis of the evaporation processes becomes possible with the video spectroscopy. Examples of the temporal evolution of the spectral radiance (without intensity cal-

ibration) in the range of Ca I lines are given in Figs. 16 and 17 for two kinds of coatings. Notice, that the evolution can be followed with a time step of 0.25 ms, and only few time instants are presented in the Figures. The evolution of the Cu I line at 42.5 nm can be used to roughly estimate the intensity of the copper dominated arc – a small increase during first microseconds is followed by an almost constant intensity of the Cu I line.

A considerable emission of the Ca I lines is observed in both cases starting already in the first microsecond. The decrease of the lines during next microseconds can be explained with effects of the gas flow; a further establishment of the copper vapour flow from the cathode which displaces the Ca vapour but also other effects in the Ca vapour flow itself.

Ca lines of increased profile width and sometimes with self-reversal can be seen in the example in Fig. 17. This promotes the conclusion that the Ca vapour pressure is much larger in the case of the coating with plaster.

The analysis of the Ca line radiation even in the case of higher optical thickness can lead to a quantitative determination of the Ca vapour and, hence, an estimation of the vapour flow. Here, the arc temperature profile estimated by spectrum simulations in the copper-air mixture can be used as a first step. However, composition calculations for the full gas mixture resulting from electrode and ceramic coating evaporation are required for more accurate determination. The final step would be radiation transport calculations for the Ca lines and a comparison with the video spectroscopy results following the approach given above. The application of such a procedure is scheduled for further research.

The thermographic studies have been used to pre-estimate the protection effect of the different coatings. Results for the temporal evolution of the surface temperature of the substrates backside are given in Fig. 18. A number of experiments have been evaluated for the same kind of coating. An appropriate selection of the temporal courses in Fig. 18, two courses in each case, illustrates also the shot-to-shot variation. Despite the variation for the same coating, a systematic difference between the coatings with organic binder and with plaster is observed. In the latter cases, only slow and low temperature increase at the backside is obtained. In contrast, a heating-up within 1 or 2 seconds up to temperatures which are 16 to 22 degree above the room temperature followed by a slow decrease is observed in the case of organic binders. Such behavior is expected because of the higher stability and lower thickness of the coatings with organic binders. The higher heating-up of the samples with $MgCO_3$ in comparison with $CaCO_3$ agrees with earlier findings [12].

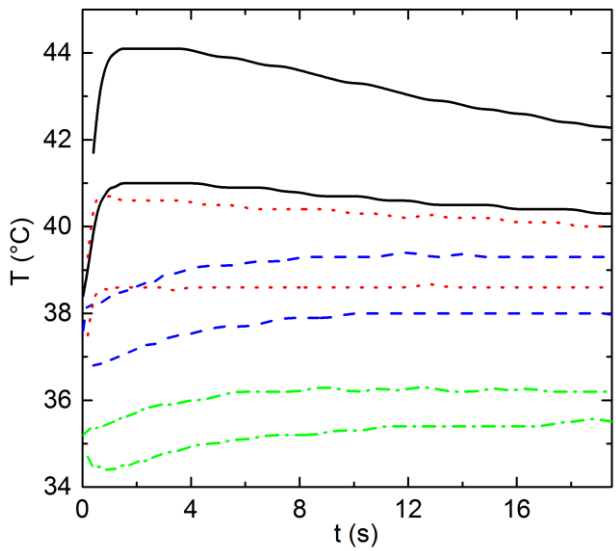

Fig. 18: Temporal evolution of the back-side surface temperature of the substrates for coatings with $MgCO_3$ + organic binder (black solid line), $MgCO_3$ + plaster (blue dashed line), $CaCO_3$ + organic binder (red dotted line), $CaCO_3$ + plaster (green dash-dotted line)

In conclusion, $CaCO_3$ coatings with plaster as a binder material provide the best protection because of a pronounced evaporation in comparison with the other cases. However, the low stability and larger inhomogeneity of simple plaster coatings represents a significant drawback. Further studies are required to find optimal coatings with a comparable protection effect and concurrently an appropriate stability.

6 SUMMARY AND OUTLOOK

A free-burning arc experiment has been used to demonstrate the application of extended methods of emission spectroscopy for the

study of arc-wall interactions. Radiation transport and plasma composition calculations are used to simulate the spectral radiance of the arc. The comparison with imaging OES represents an interesting way to estimate spatial profiles of the arc temperature and species densities including vapour densities of eroded material.

Exemplary results have been presented for the radial arc temperature profile and the profile of the copper vapour pressure caused by significant electrode erosion. The power loss by the emitted radiation and finally the expected heat load of sidewalls have been estimated from these results. The additional analysis of vapour pressures of eroded wall material, resulting from ceramic layers for example, need more complex composition and radiation transport calculations. This will be subject of future work. The complementary use of video spectroscopy has been illustrated in the paper. This enables an interesting way to study the dynamics of arc temperature and vapour distributions which allows conclusions on the evaporation processes.

Simple ceramic coatings represent a specific option for the heat protection of sidewalls in switch gear because of the strong evaporation under impact of arc radiation. A future use requires additional improvement of coating techniques and the use of binders.

REFERENCES

[1] Tanaka Y, Yokomizu Y, Ishikawa M, Matrumura T, Kito Y, Phys. D: Appl. Phys. 30 (1997) 407-416.

[2] Kozakov R, Kettlitz K, Weltmann KD, Steffens A, Franck CM, J. Phys. D: Appl. Phys. 40 (2007) 2499-2506.

[3] Wiese W L, Spectrochimica Acta 46B (1991) 831-841.

[4] Schneidenbach H, Franke St, J. Phys. D: Appl. Phys. 41 (2008) 144016.

[5] Wendt M, Franke St, J. Phys. D: Appl. Phys. 41 (2008) 144018.

[6] Seeger M, Tepper J, Christen T, Abrahamson J, J. Phys. D: Appl. Phys. 39 (2006) 5016-5024.

[7] Lee A, Heberlein J V R, Meyer T N, IEEE Trans. Components, Hybrids, and Manufacturing Technol. 8 (1985) 129-134.

[8] Rodriguez P, Didier J, Bernard G, Rowe S, IEEE Trans. Power Delivery 13 (1998) 480-488.

[9] Tanaka Y, Shinsei N, Amitani K, Uesugi Y, Wada J, Okabe Sh, IEEE Trans. Plasma Sci. 39 (2011) 2776-2777.

[10] Jonsson E, Runde M, Dominguez G, Friberg A, Johansson E, IEEE Trans. Power Delivery 28 (2013) 2065-2070.

[11] Onchi T, Yanase H, Yamazaki M, Kuroda M, Isozaka M, Sugiyama Sh, Hata J, Yonemitsu K, IEEJ Trans. PE 127 (2007) 692-698.

[12] Uhrlandt D, Gorchakov S, Brüser V, Franke St, Khakpour A, Lisnyak M, Methling R, Schoenemann Th, J. Phys.: Conf.Series 550 (2014) 012010.

[13] Franke St, Methling R, Uhrlandt D, Bianchetti R, Gati R, Schwinne M, J. Phys. D: Appl. Phys. 47 (2013) 015202.

[14] Lochte-Holtgreven W, Plasma Diagnostics, North-Holland Publishing Company, Amsterdam, 1968.

[15] Peytremann E, A&A 17 (1972) 76.

[16] Sahal-Brechot S, Segre ERA, A&A 13 (1971) 161.

[17] Verner D A, Yakovlev D G, A&AS 109 (1995) 125.

[18] Verner D A, Ferland G J, Korista K T, Yakovlev D G, Astrophys. J. 465 (1996) 487.

[19] Kasyanow W, Starosting A, Sov. Phys. – JETP 21 (1965) 193.

[20] Cressault Y, Gleizes A, J. Phys. D: Appl. Phys. 46 (2013) 415206.